Unsteady and three-dimensional aerodynamic effects on wind turbine rotor loads

Arturo Muñoz-Simón*, Andrew Wynn† and Rafael Palacios‡
Imperial College London, UK, SW7 2AZ

The paper investigates the use of vortex methods in the computation of important flows for wind turbine aerodynamics. These flows are characterised by inflow velocity unsteadiness, spatial variations and non-zero spanwise component. First, computational vortex methods are shown to match analytical solutions on simple geometries. Second, these geometries will be studied to reveal the effects of these flows on airfoil aerodynamics: unsteady damping and load reduction when subjected to side slip or spanwise inflow velocity variations. Finally, vortex methods will be compared with traditional BEM methods in full wind turbine configurations under real operating inflows such as shear, yaw and turbulence which are characterised by unsteadiness and three-dimensional effects. Vortex methods allow quantifying the error of BEM methods for these conditions.

Nomenclature

$\mathcal{AR}$	=	Aspect ratio
C_L, C_D, C_M	=	Lift, drag and moment coefficients
C_{L_α}	=	Slope of the C_L vs. α curve
$C_{L_{ss}}$	=	C_L in steady state
C_s	=	Span coefficient
C_T, C_N	=	In and out-of-plane force coefficients
C_{th}	=	Thrust coefficient of the rotor
C_p	=	Power coefficient of the rotor
R	=	Rotor radius
r	=	Radial coordinate
r^*	=	Non-dimensional radial coordinate
t^*	=	Non-dimensional time
U_∞	=	Wind speed
U_r	=	Relative incoming velocity with respect to the airfoil
α	=	Angle of attack
α_{L0}	=	Angle of attack at which $C_L = 0$
γ	=	Shear coefficient
θ	=	Azimuthal angle
λ	=	Wavelength of the incoming velocity along the span
Λ	=	Side slip angle in airfoils
ψ	=	Küssner function
Ψ	=	Yaw angle
ϕ	=	Wagner function
$\boldsymbol{\xi}$	=	Vorticity

*Early Stage Researcher, Department of Aeronautics, a.munoz-simon@imperial.ac.uk
†Senior Lecturer in Control, Department of Aeronautics, a.wynn@imperial.ac.uk
‡Professor of Computational Aeroelasticity, Department of Aeronautics, r.palacios@imperial.ac.uk, AIAA Associate Fellow

I. Introduction

Aerodynamic effects such as unsteadiness and three-dimensional effects are currently gaining importance in wind turbine analysis. The need for their consideration has been strengthen by the increasing length and flexibility of the blades [1], floating platforms, complex terrains and new control strategies that exploit the interaction between wind turbines and upstream wakes [2]. As a consequence, computational methods need to be upgraded or new ones need to be created. Currently, Blade Element Momentum (BEM), vortex methods, Unsteady Reynolds-Averaged Navier-Stokes (URANS) and Actuator Line - Large Eddy Simulation (AL-LES) are the available fidelities [3].

BEM theory is widely employed [4] and constitutes the standard method for industry [5]. It uses two-dimensional steady airfoil data to compute wind turbine performance under the hypothesis of steady flow and independent two-dimensional blade sections [6]. In the present article, any aerodynamic phenomenon that implies interaction between blade sections is considered to experience a "three-dimensional effect" and any phenomenon with variations in time is called an "unsteady effect". However, in practice, empirical corrections are typically applied to approximate wind turbine behaviour under these conditions [7, 8]. These corrections are created from higher fidelity methods or from experiments and are usually not sufficiently general to capture the full range of possible turbine dynamics [9, 10].

Vortex methods [11, 12] are less commonly used in the computation of wind turbine aerodynamics. In general, they assume inviscid and incompressible flow implying that no effects associated with viscosity (friction drag and separation) or compressibility can be accounted for. Some authors have overcome these restrictions [13, 14] but they have not been dealt with in this paper that focus on primary effects.

Other methods such as URANS or blade-resolved LES are able to overcome the drawbacks of both BEM (unsteadiness and three-dimensional effects) and vortex (viscosity and compressibility) methods [10, 15, 16]. However, they are still not computationally efficient enough to support aerodynamic analysis at the design phase.

Unsteady and three-dimensional effects appear naturally in wind turbine aerodynamics under real operating incoming flows. Unsteadiness appears at different characteristic frequencies in different flows: at the rotation frequency in shear and yaw and associated to the wind spectrum in turbulence. Spanwise flow occurs in cases of yaw and to a lesser extent in turbulence. Finally, spanwise variations appear in shear (large wavelength) and turbulent (shorter wave lengths) flows. Concurrently, these effects appear also in airfoil aerodynamics. Traditionally, gusts have been employed as an example of unsteadiness. Moreover, side slip cases generate spanwise flow and spanwise-varying incoming velocity cases give rise to three-dimensional flow.

Airfoils represent a simple geometry that sometimes accepts analytical solutions constituting a valuable source of information for code validation. Specifically, small perturbation theory [17] has been used to characterise the unsteady behaviour of two dimensional airfoils and lifting-line theory [12] has been used to analyse three-dimensional effects. These are vortex theories that can be automatically extended to complex geometries through a computational implementation which is usually very efficient [12]. In particular, the present paper uses panel methods on thin airfoils known as Unsteady Vortex Lattice Method (UVLM).

In this paper, vortex methods will be used to improve the understanding of wind turbine aerodynamics and the limitations of BEM methods under these flows. First, section II includes the description of these methods. Afterwards, the main aerodynamic features of these flows will be studied on basic geometries for validation and to provide a systematic analysis of unsteady and three-dimensional effects (section III). Finally, the aerodynamics of a reference 10MW wind turbine rotor under realistic operation flows (yaw, shear and turbulence) will be computed with vortex and BEM methods for comparison (section IV).

II. Computational methods

This section describes the very basic theory behind two methods that will be used further on and their implementations. Each of them is a state-of-the-art representative of some of the fidelities described in section I: BEM and vortex methods.

A. Blade Element Momentum

BEM theory [6] is based on the connection of two theories. The *momentum theory* treats, initially, the rotor as a porous disc. The mass conservation equation of this system can be written as

$$\rho A_\infty U_\infty = \rho A_d U_d = \rho A_w U_w, \tag{1}$$

where U_∞, U_d and U_w are the flow velocities infinitely upstream of the rotor, at the rotor plane and in the wake, respectively. The traditional definition of the induction a is used

$$U_d = U_\infty(1 - a). \tag{2}$$

Moreover, the force on the porous disc can be related to the momentum loss of the flow across the disc

$$(p_d^+ - p_d^-)A_d = (U_\infty - U_w)\rho A_d U_\infty(1 - a), \tag{3}$$

where p_d^+ and p_d^- are the pressure immediately upstream and downstream the rotor, A_d is the rotor area and ρ is the fluid density. The flow pressures and velocities are also related by the Bernoulli equation that should be applied separately upstream and downstream the rotor

$$\frac{1}{2}\rho U_\infty^2 + p_\infty = \frac{1}{2}\rho U_d^2 + p_d^+, \tag{4a}$$

$$\frac{1}{2}\rho U_w^2 + p_\infty = \frac{1}{2}\rho U_d^2 + p_d^-, \tag{4b}$$

where p_∞ is the flow pressure infinitely away from the rotor. Equations (1), (2), (3) and (4) can be combined to obtain the velocity in the wake

$$U_w = (1 - 2a)U_\infty. \tag{5}$$

Under the assumption of independent radial sections of the rotor, the momentum theory described above can be applied separately to each radial annulus such that it can be related with the second theory that BEM methods use, the *rotor blade theory*. This theory defines the aerodynamic forces in each annulus of the rotor (δL and δD) based on the local velocity (U_r) and the two-dimensional aerodynamic data known beforehand (C_L and C_D), which is usually obtained from wind tunnel measurements of computational methods

$$\delta L \cos\phi + \delta D \sin\phi = \frac{1}{2}\rho U_r^2 N c(C_L \cos\phi + C_D \sin\phi)\delta r, \tag{6}$$

where δ represents variations along the radial coordinate r, L and D are, respectively, the airfoil lift and drag forces with associated non-dimensional coefficients C_L and C_D, ϕ is the flow angle, U_r is the relative velocity, N is the number of blades and c is the section chord. The combination of the two previous theories and the appropriate geometrical relationships between velocities give rise to a system of equations that can be iteratively solved to obtain velocities and forces.

There are some further details needed to complete the method such as the angular momentum equation [6]. Moreover, important three-dimensional and unsteady effects are missing, forcing this method to use semi-empirical corrections [18] for rotation, tip and root ends and wake deviation effects. Usually, these corrections are adjusted for the most simple cases leading to miscalculations in the most complex ones [10] such as unsteady inflow or large yaw angles. Efficiency is the main advantage of this method.

OpenFAST is the open-source [19] version of FAST (Fatigue, Aerodynamics, Structures and Turbulence) [20, 21] which is the aeroelastic code for horizontal-axis wind turbines of the National Renewable Energy Laboratory (NREL). It uses a BEM model for the steady aerodynamics with different corrections [6] and options for the unsteady behaviour. For the structural dynamics it provides linear and non-linear theories.

B. Vortex methods

Vortex methods are based on the inviscid and incompressible flow equations [12, 22]

$$\begin{cases} \nabla \cdot \boldsymbol{u} = 0 & \text{in} \quad \Omega \\ (\boldsymbol{u} - \boldsymbol{u}_{\partial\Omega_s}) \cdot \boldsymbol{n} = 0 & \text{at} \quad \partial\Omega_s \\ \boldsymbol{u} = \boldsymbol{U}_\infty & \text{as} \quad |\boldsymbol{x}| \to \infty, \end{cases} \tag{7}$$

where $\boldsymbol{u}$ is the flow velocity (whose value is $\boldsymbol{U}_\infty$ infinitely far away from the solid surfaces), $\boldsymbol{n}$ is the normal vector to the solid surfaces, $\Omega \subset \mathbb{R}^3$ is the fluid domain with $\partial\Omega_s$ solid boundaries.

However, equation (7) can be reformulated using the relationship between velocity and vorticity ($\boldsymbol{\xi} = \nabla \times \boldsymbol{u}$) and applying Green's theorem. The advantage of writing the equations based on the vorticity becomes obvious considering that the vorticity will be generated in the boundary layer of solid surfaces [22], shed to the flow at the trailing edge and convected downstream giving rise to the wake. Thus, only the 2D vorticity field should be solved in solid surfaces and wakes under the following boundary conditions

$$(\boldsymbol{u} - \boldsymbol{u}_{\partial\Omega_s}) \cdot \boldsymbol{n} = 0 \quad \text{at} \quad \partial\Omega_s, \tag{8a}$$

$$\Delta p|_{\partial\Omega_w} = 0 \quad \text{at} \quad \partial\Omega_w, \tag{8b}$$

$$\boldsymbol{u} = \boldsymbol{U}_\infty \quad \text{as} \quad |\boldsymbol{x}| \to \infty, \tag{8c}$$

where, now, $\partial\Omega$ includes solid $\partial\Omega_s$ and wake $\partial\Omega_w$ boundaries. First, the non-penetration condition between the flow and the solid surfaces is provided by Equation (8a). Second, Equation (8b) assures that the wake does not carry any load. Finally, Equation (8c) enforces the boundary condition at infinity.

The wake convection admits two modelling fidelities. If the vorticity is convected by the inflow velocity, the wake is said to be "prescribed" because its shape can be known in advance. However, if the vorticity is convected by the inflow velocity plus the velocity induced by the rest of the vorticity, it is named "free wake". The first approximation is much more computationally efficient [23].

In the present article, the UVLM method will be used [24]. It assumes low thickness-to-chord ratio to further simplify the surfaces as zero-thickness. It discretises the equations and uses Biot-Savart law for the computation of induced velocities

$$\boldsymbol{u}_{\text{ind}_{ij}} = \frac{\Gamma_j}{4\pi} \sum_{k=1}^{4} \frac{\boldsymbol{dl}_k \times \boldsymbol{r}_{ik}}{|\boldsymbol{r}_{ik}|^3}, \tag{9}$$

where $\boldsymbol{u}_{\text{ind}_{ij}}$ is the induced velocity on point i by the vortex j which is composed by four segments indexed by k with length $\boldsymbol{dl}$ and strength Γ.

After solving the vorticity fields, the velocity can be reconstructed and the forces can be computed. The steady and unsteady forces will be computed with the Kutta-Joukowsky theorem and the unsteady term in the unsteady Bernoulli equation, respectively,

$$\boldsymbol{F}_i = \rho\Gamma\boldsymbol{u}_i \times \boldsymbol{dl}_i + \rho\frac{\partial\Gamma_i}{\partial t} \cdot \boldsymbol{dl}_i. \tag{10}$$

In this case, depending on the wake convection fidelity chosen, the wake is convected via either one of the following two conditions

$$\Delta\boldsymbol{x} = \boldsymbol{U}_\infty \cdot \Delta t \qquad \text{Prescribed wake} \tag{11a}$$

$$\Delta\boldsymbol{x} = (\boldsymbol{U}_\infty + \boldsymbol{u}_{\text{ind}}) \cdot \Delta t \qquad \text{Free wake} \tag{11b}$$

SHARPy stands for Simulation of High Aspect Ratio Planes in Python [25] and it is an aeroelastic code developed by the authors in collaboration with the team in Imperial College London [26, 27]. The aerodynamics are captured with an UVLM [24] that accounts for three-dimensional and unsteady effects but neglects viscosity, compressibility and body thickness. The aerodynamic solver includes steady (through horseshoe or discretised wake) and unsteady (with prescribed or free wake) solutions. The structural dynamics are described through the geometrically exact beam theory (GEBT) that is able to account for the six degrees of freedom of each section as well as for the anisotropy of composite materials giving rise to a non-linear beam model [28]. Moreover, multibody features are simulated though joints implemented as Lagrange multipliers constraints using the formulation of Ref. [29].

III. Airfoil aerodynamics

The objective of this section is twofold. First, analytical solutions for simple airfoil geometries under complex inflow conditions will be used to validate the aerodynamic computations of SHARPy. Second, these unsteady

and three-dimensional inflows will be systematically analysed with SHARPy to explain how they affect the airfoil performance. It reveals key features of the unsteady and three-dimensional flows that will be useful to understand how these scenarios influence wind turbine rotor aerodynamics in section IV and the suitability of vortex and BEM methods to simulate it.

A. 2D Unsteadiness

Unsteadiness in wind turbine aerodynamics originates from a variety of sources such as aeroelastic couplings, wind fluctuations, separation or transition. BEM methods account for unsteadiness through dynamic wake models [3] and unsteady airfoil aerodynamics [7]. Vortex methods can inherently account for it and it has traditionally been studied through gust response [17] at first level. A suitable scale to measure the unsteady effects is the convective time scale which is generated using the airfoil semi-chord and the relative velocity

$$t^* = \frac{t \cdot U_r}{c/2}, \tag{12}$$

where t^* is the non-dimensional time, t is time, U_r is the relative velocity to the airfoil and c is the airfoil chord.

1. Validation

Small perturbation theory [17] provides the analytical lift response of 2D airfoils to different types of gusts. A Küssner gust is a sudden step in the vertical component of the inflow that is convected by the incoming wind velocity along the airfoil generating the following time history of the lift coefficient

$$C_L(t^*) = 2\pi\Delta\alpha(0)\psi(t^*), \tag{13}$$

where C_L is the lift coefficient, t^* is the non dimensional time, $\Delta\alpha$ is the change in angle of attack and ψ is the Küssner function. On the other hand, a Wagner gust is a sudden change in the incoming velocity that applies to the whole flow field at the same time. This generates the following response

$$C_L(t^*) = 2\pi\Delta\alpha_{3c/4}\phi(t^*), \tag{14}$$

where C_L is the lift coefficient, t^* is the non dimensional time, $\Delta\alpha_{3c/4}$ is the change in angle of attack measured at $3/4$ of the chord and Φ is the Wagner function.

The airfoil model based on thin-airfoil theory constitutes a linear dynamical system whose frequency response can be computed and approximated with a state-space representation of the system through rational function approximation. In this context, the Küssner and Wagner functions are obtained from the system response to a step in the incoming velocity or the airfoil pitch, respectively. In the present work, 10 states were enough to reach convergence and thus, this approximation of the system was used.

For the validation (Fig. 1) both Küssner and Wagner gusts have been computed for a flat plate at initially zero angle of attack and a gust step of $0.1\,^\circ$. SHARPy reproduces the behaviour accurately for both gusts with an error below 1% after the noise in the first time steps. The noise is associated to the computation of the unsteady force (10) which requires the approximation of the time derivative of the circulation which is infinite in the analytical solution.

The upwind discretisation of the wake convection equation with a first order approximation imposes a maximum CFL of one. Due to the numerical discretisation of the wake it is automatically assured in the wake region. However, it has to be enforced in the vorticity shedding step making the last bounded panel equal to the first wake panel in the flow direction [30]. Moreover, the implementation of the unsteady Kutta condition that provides the best results is setting the vorticity of the first wake panel equal to the vorticity in the last bounded panel at the previous time step [31].

2. Analysis

The computation of gusts on airfoils is the first step towards the characterisation of unsteady effects on full rotor configurations. For that reason, it is interesting to compute continuous varying velocity inflows. With that objective,

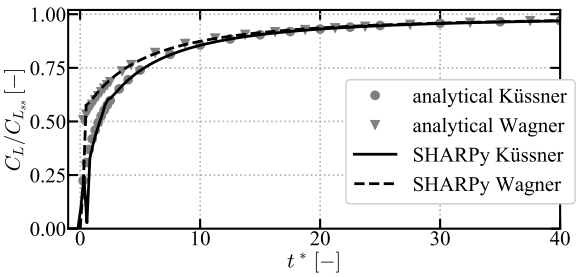


Fig. 1 Küssner and Wagner gusts over an airfoil

a convolution integral can be applied to generate an analytical solution for continuous turbulence [17] based on the previous solution for Küssner gusts (13)

$$C_L(t^*) = 2\pi\alpha(0)\psi(t^*) + 2\pi\int_{0^+}^{t^*}\frac{d\alpha}{d\tau}\psi(t^*-\tau)d\tau, \tag{15}$$

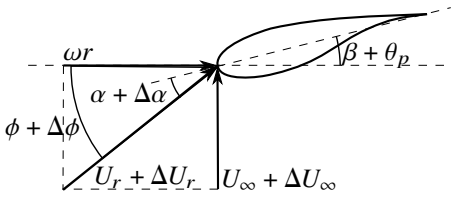
where C_L is the lift coefficient, t^* is the non dimensional time, α is the angle of attack and ψ is the Küssner function.

Continuous turbulence has been analysed on an airfoil whose characteristics (twist $\beta = 4.52°$, pitch $\theta_p = 0°$, chord $c = 3.41\,m$, blade velocity $\omega r = 72.92\,m/s$ and inflow velocity $U_\infty = 10.5\,m/s$) have been obtained from the spanwise position r/R=0.75 of the AVATAR wind turbine that will be described in section IV.A. The turbulence has been introduced in the system though the incoming wind velocity (U_∞) which will generate a change in the angle of attack according to the geometric relationships in Figure 2a, specifically

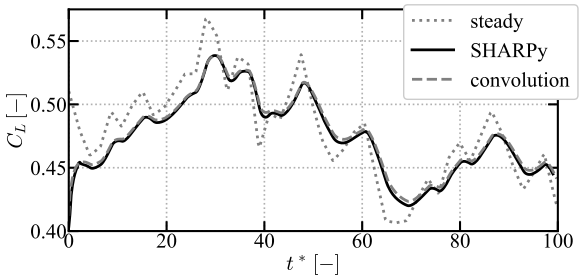
$$\alpha + \Delta\alpha = \arctan\left(\frac{U_\infty + \Delta U_\infty}{\omega r}\right) - \beta - \theta_p. \tag{16}$$

The time series of the inflow velocity has been obtained from the hub height probe of a turbulent field generated according to IEC-KAI level A with Turbsim [32].

Fig. 2b shows a good agreement between SHARPy and the analytical solution (Eq. (15)). Moreover, the importance of unsteadiness is revealed through the comparison between the previous solutions and the steady approximation. The unsteady signal is smoother and slightly delayed with respect to the steady approximation. This effects highlights the importance of having an adequate unsteady model to capture the flow unsteadiness in rotor aerodynamics (section IV.E).



(a) Scheme



(b) Lift response

Fig. 2 Turbulent inflow on an airfoil

3. Unsteady time scale

The airfoil response to gusts also provides valuable information to evaluate whether a certain phenomenon will trigger the unsteadiness or can be approximated by the quasi-steady behaviour. As illustrated in Figure 1, after non-dimensional

time around 15, the airfoil response to unsteadiness is very close to the steady state (difference below 10%). Any phenomenon with characteristic time below 15 will have an important interaction with aerodynamic unsteadiness. Some characteristic time scales on the AVATAR wind turbine can therefore be converted into the time scale of equation (12) to check if they fall in the unsteady region.

The blade-passing frequency (that would be characteristic of shear loads) of the AVATAR wind turbine is between 10 and 100 non-dimensional time units. The first flap wise natural frequency is between 5 and 50 [33]. And, finally, the wind spectrum based on IEC has characteristic time steps larger than 20. This shows that the most important unsteady aerodynamic effects are more likely to be originated by the aeroelastic coupling rather than the wind fluctuations in this case.

B. Spanwise flow

Wind turbine blades are always subjected to spanwise flow due to the variations in loading along the span. In the root region, the dominant source of spanwise flow is separation and is usually corrected in BEM methods. Spanwise flow is usually not addressed in the tip region where the behaviour is dominated by the tip-loss correction [6]. In yawed rotors, spanwise flow is of primary importance and cannot be tackled by the previous corrections, thus, it has to be further corrected by engineering approximations [8, 34]. On the other hand, vortex methods can inherently account for this effect. While this effect will be very complex in the 3D wind turbine configuration (section IV) a first investigation to the problem can be done through flying wings under side slip.

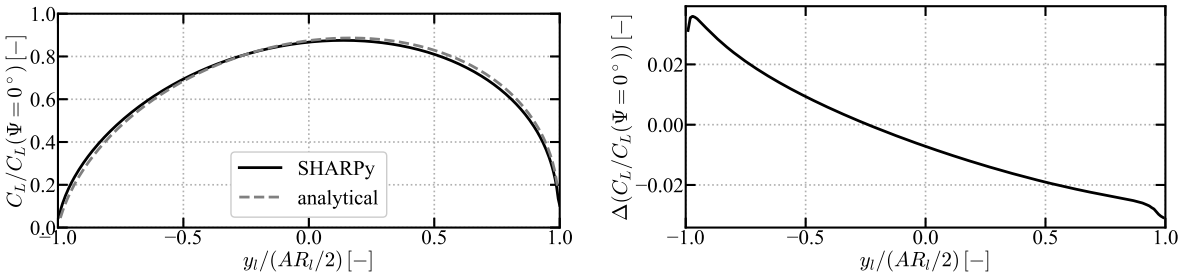
1. Validation

Lifting-line theory [12] provides the lift and drag coefficient of elliptic wings under no side slip for a certain aspect ratio AR. The extension of this theory for oblique wings [35] generates an analytical solution of the lift on wings under oblique inflow. In this case, an elliptic wing will be used for validation

$$\begin{aligned}\frac{C_L}{8\cos(\Lambda)\alpha} =& \sqrt{1-y_l^2}\left(1-\frac{\pi}{2\mathit{AR}_l}\right)-\frac{\sin\Lambda}{\mathit{AR}_l}\sqrt{1-y_l^2}\sin^{-1}y_l \\ &+\frac{\sin\Lambda}{\mathit{AR}_l}y_l\left(\ln 8\mathit{AR}_l\sqrt{1-y_l^2}-(1-2k)-\csc\Lambda\left(\ln|1+\sin\Lambda|-(1-\sin\Lambda)\ln|\cos\Lambda|\right)\right),\end{aligned} \tag{17}$$

where C_L is the lift coefficient, Λ is the side slip, α in the angle of attack, y_l is the spanwise coordinate projected on the flow direction with AR_l associated aspect ratio and k is the straight axis location as a function of the chord.

The lift estimation of SHARPy agrees very well with the theoretical solution (Eq. (17)) in value and maximum position (Fig. 3a). A small difference occurs between both estimations towards the wing edges (Fig. 3b), which can be explained from the lack of chordwise information in the lifting line model.



(a) Lift distribution along span **(b) Lift difference**

Fig. 3 Sectional lift on an elliptic wing with oblique inflow (45°)

Numerically, the bounded panels in the UVLM have to be placed parallel to the incoming flow to get the most accurate results.

2. Analysis

The effect of yaw on wings will be analysed through two variables: the maximum lift coefficient C_{Lmax} and its position along the span $y(C_{Lmax})/b$ where b is the semi-span. As pointed out by the validation case, the maximum lift coefficient decreases and displaces out of the mid position. Figure 4 shows how this effect is stronger the larger the yaw angle. Moreover, it shows the weak effect of the aspect ratio on the maximum lift coefficient decay and how the smaller the aspect ratio the quicker the displacement of the maximum position with the yaw angle. It is important to capture this effect because it will appear in wind turbines under yaw (section IV.D). Furthermore, it will be complemented by the *advancing/retreating* and the *skew wake* three-dimensional effects.

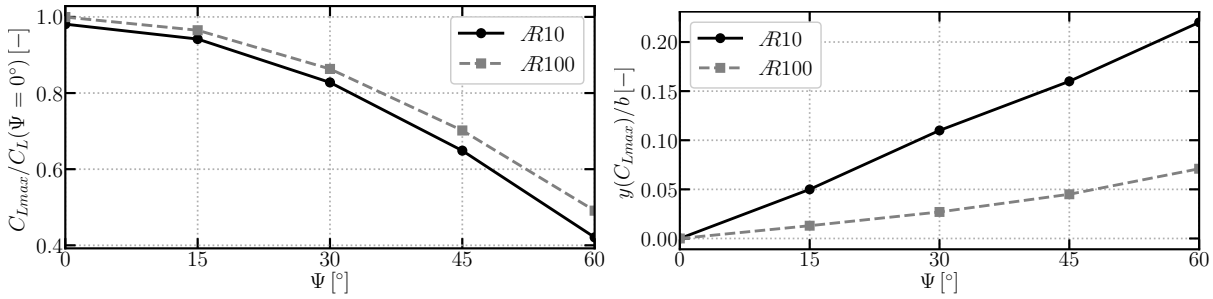


Fig. 4 Side slip effect on section lift coefficient value and position

C. Spanwise variations of the inflow velocity

In cases of inflow turbulence there are spanwise variations of the incoming velocity that will, consequently, generate spanwise varying loads. This scenario is against the fundamental hypothesis of BEM methods and is usually ignored. Vortex methods can inherently account for this effect and will be used to systematically study these cases on airfoil geometries before computing the full wind turbine configuration. In section IV.E this will be seen to have a huge effect for uncorrelated inflows on large rotors.

1. Validation

Lifting-line theory [22] provides, again, an analytical solution for the steady aerodynamics of finite-span wings under arbitrary incoming flow based on a spanwise parametrisation complying with the change of variable

$$y = b\cos\Theta, \tag{18}$$

where b is the semi-span, y is the coordinate along the span and Θ is the parameters of the change of variables.

This solution consists of a Fourier series decomposition of the circulation along the airfoil whose coefficients should be resolved to meet the equilibrium between incoming and induced angles of attack

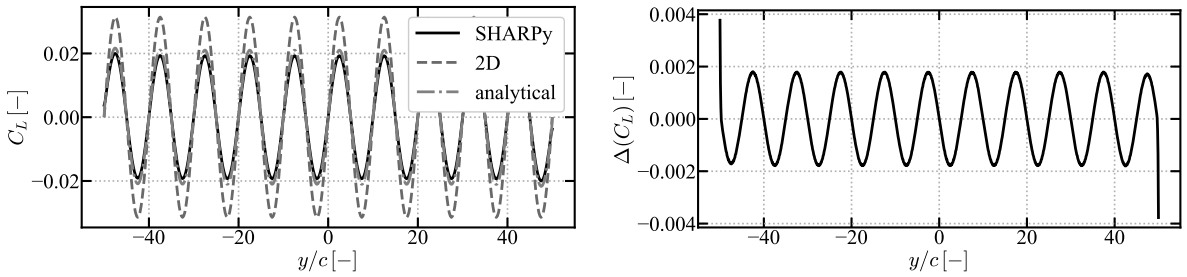
$$\frac{8b}{C_{L\alpha}(\Theta)c(\Theta)}\sum_{n=1}^{\infty}A_n\sin(n\Theta) + \sum_{n=1}^{\infty}nA_n\frac{\sin(n\Theta)}{\sin\Theta} = \alpha(\Theta) - \alpha_{L0}(\Theta), \tag{19}$$

where b is the semi-span, C_{L_α} is the lift vs. angle of attack curve slope, c is the airfoil chord, α is the angle of attack, α_{L0} is the angle of attack of zero lift and n and A_n are, respectively, the index and coefficients of the Fourier series expansion.

The validation has been done for a wing of $\mathcal{A}R = 100$, with $\lambda = 10c$ in a gust amplitude of 0.01 with respect to the average incoming velocity. In particular, 500 harmonics of the lifting line have been computed through a least squares approximation of 1500 sampling points. The difference between the UVLM and the lifting line solution is below 10% (Fig. 5).

2. Analysis

Figure 6 shows an example of the force coefficients variation along the span. The lift average value does not vary but its peak-to-peak value (indicated with angle brackets $\langle\bullet\rangle$ from now on) is reduced with respect to the 2D hypothesis.



(a) Lift along the span **(b) Lift difference between SHARPy and lifting line**

Fig. 5 Sectional lift due to spanwise-varying incoming normal velocity on a slender wing ($\mathcal{AR}$ = 100)

Moreover, average drag appears with a net value above zero. Finally, zero-average moment and spanwise coefficients appear with small peak-to-peak variations.

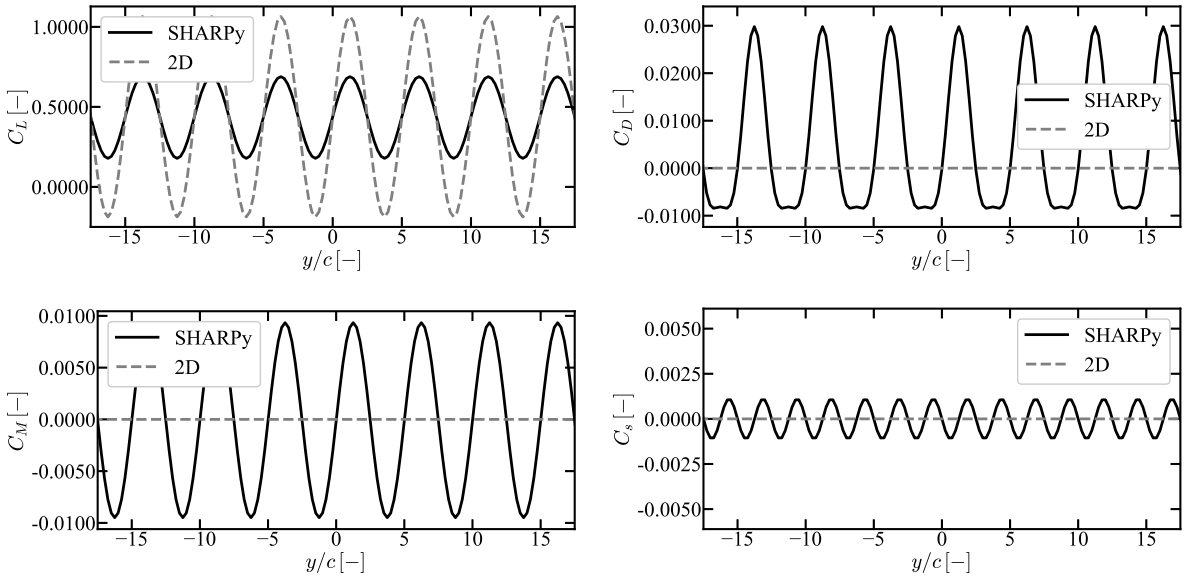
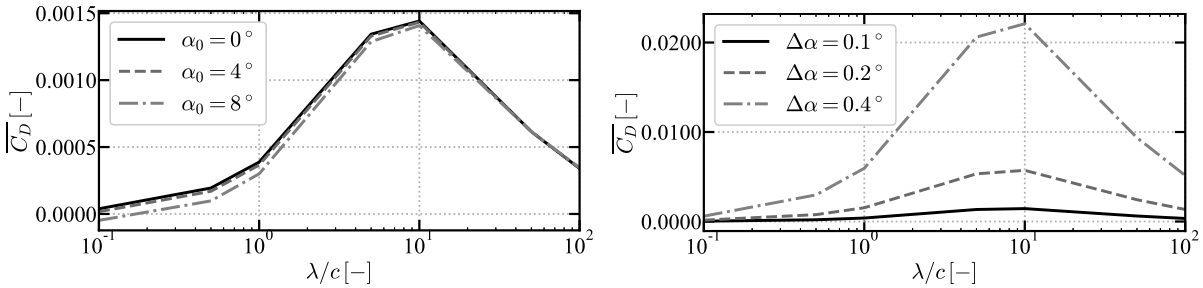


Fig. 6 Spanwise coefficients under spanwise sine varying inflow. α_0 = 4° with $\Delta\alpha$=0.2°

The characteristic spatial scales of the phenomena in wind turbines are very wide ranging from the smallest spatial scale of wind turbulence to the blade length. For this reason, and based on the previous example, this effect will be systematically studied generating a spanwise distribution of a certain wavelength on a simple airfoil geometry. Figure 7 and 8 show the influence of the wavelength of the incoming flow on the airfoil coefficients average ($\overline{\bullet}$) and peak-to-peak ($\langle\bullet\rangle$) values, respectively. In particular, Figs. 7a and 8a show the influence of the angle of attack and Figs. 7b and 8b the influence of the gust intensity.

On the one hand, the average lift, moment and spanwise coefficients are zero (not shown). However, Fig. 7 shows an average non-zero drag coefficient around 100-200 drag counts which is comparable to the usual drag value of airfoils. It reaches a maximum for wavelengths of the order of ten chords with larger value the larger the gust intensity but almost unaffected by the average angle of attack.

Finally, Figure 8 shows the variation of the peak-to-peak coefficients. The variation of peak-to-peak lift coefficient with respect to the equivalent 2D variations is very significant. This reduction is around 40% for inflow wavelength

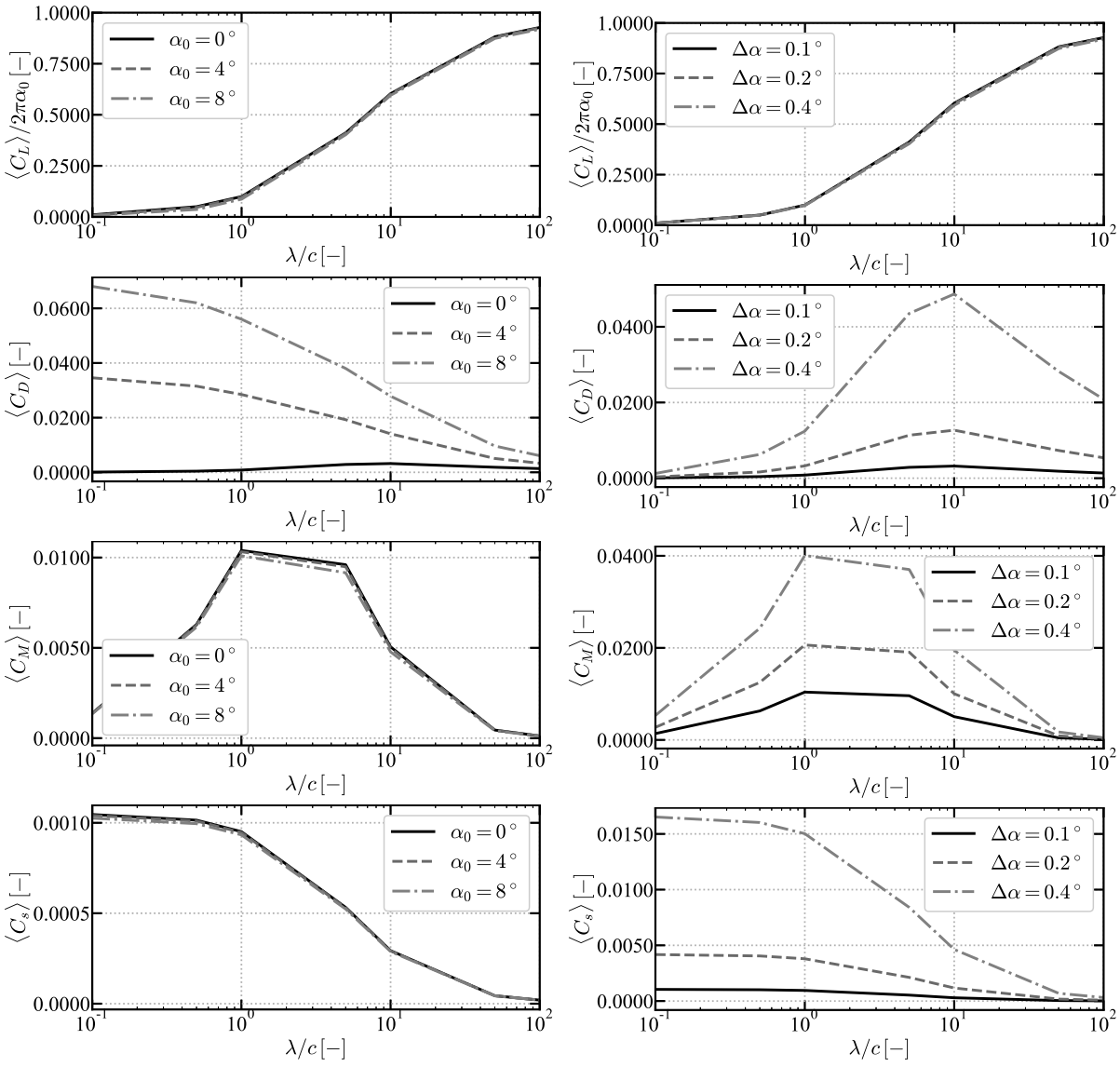


(a) Angle of attack effect for $\Delta\alpha$ = 0.1°

(b) Gust intensity effect for α_0 = 0°

Fig. 7 Effect of the inflow spanwise wavelength on the average airfoil drag

equal to 10 times the chord length and around 90% for wavelengths of the order of the chord. However, this effect is not influenced by the initial angle of attack or the gust intensity. The behaviour of the peak-to-peak drag coefficient is not well defined as a function of the wavelength because it depends on a balance between the average angle of attack and the gust intensity. The peak-to-peak moment and spanwise coefficients reach the maximum for wavelengths of the order of 0.1 chords. These two coefficients are slightly affected by the initial angle of attack but they both increase with the gust intensity. Their values are small but could be significant for certain airfoils.



(a) Angle of attack effect for $\Delta\alpha = 0.1°$ **(b) Gust intensity effect for $\alpha_0 = 0°$**

Fig. 8 Effect of the inflow spanwise wavelength on the airfoil coefficients peak-to-peak

IV. Wind turbine rotor aerodynamics

All the effects introduced above occur in wind turbine rotor aerodynamics and can be triggered by different sources. In this paper, they will be triggered by the inflow wind because it is a traceable method that allows the comparison between different theories. The following variables will be used in figures and tables: $r^* = r/R$ is the non-dimensional radial coordinate, C_N/dr^* and C_T/dr^* are, respectively, the out-of-plane and in-plane force coefficient per unit non-dimensional span and C_p and C_{th} are the rotor power and thrust coefficient, respectively. In some graphics their average ($\overline{\bullet}$) and standard deviation ($\sigma(\bullet)$) computed along one revolution will be shown. Moreover, some values will be presented relative to the uniform wind case and will be identified by a Δ symbol. These variables will be plotted along the radial direction or along a revolution as a function of the rotor azimuth angle (θ) which is considered zero at the top position for the first blade.

A. Model description

The AVATAR wind turbine is a benchmark case for large offshore wind turbines [36]. Its main characteristics are: 10 MW of nominal power, 102.88 m rotor radius and 137.5 m hub height. In this case, no prebending or presweep are applied [33]. The operation point has been chosen at the end of the optimal production region of the power curve, namely an incoming wind speed of 10.5 m/s and a rotation velocity of 0.945 rad/s which implies a tip-speed ratio of 9.26. At this point, the blade pitch is zero. All simulations have been run with a time step equivalent to an azimuthal progress of 0.5 ° during 5 revolutions to assure convergence.

In SHARPy simulations, blades are discretised with 14 elements in the spanwise direction starting from the hub centre, as shown in Fig. 9. Moreover, the wake length used is equivalent to five rotor revolutions and it convects downstream based on the external velocity, not accounting for self-induction (prescribed wake). The simulations include unsteady force contribution through the time-dependent term in the unsteady Bernoulli equation.

The following modifications were performed on the blade geometry (Fig. 9) due to discretisation constraints associated to the UVLM that were described in section III.A. The real blade has been created based on cambered airfoils. However, due to constraints in the geometry discretisation, the camber could not be properly modelled because panels needed to be too large near the trailing edge. For that reason, plain airfoils have been employed to build the computational blade. According to thin airfoil theory [37], the camber has two effects on airfoil behaviour: modifying the angle of zero lift and the pitch coefficient. To replicate these effects, the twist of the blade has been modified and a pitching moment has been included. To make the uncambered airfoils generate the same lift as the original cambered ones at a certain incidence, the pitch has been reduced by an angle equal to the angle of zero lift of the cambered airfoil

$$\alpha_{L0} = \int_0^1 \frac{z}{c} f_1\left(\frac{x}{c}\right) \frac{dx}{c} \quad \text{with} \quad f_1\left(\frac{x}{c}\right) = \frac{1}{\pi\left(1-\frac{x}{c}\right)\sqrt{\frac{x}{c}\left(1-\frac{x}{c}\right)}}. \tag{20}$$

Moreover, the constant moment coefficient has been computed as

$$C_{M_{c/4}} = 2\mu_0 - \frac{\pi}{2}\alpha_{L0} \quad \text{with} \quad \mu_0 = \int_0^1 \frac{z}{c} f_2\left(\frac{x}{c}\right) \frac{dx}{c} \quad \text{and} \quad f_2\left(\frac{x}{c}\right) = \frac{1-2\frac{x}{c}}{\pi\left(1-\frac{x}{c}\right)\sqrt{\frac{x}{c}\left(1-\frac{x}{c}\right)}}. \tag{21}$$

In the previous equations, the camber line is defined through the x and z coordinates which are parallel and perpendicular to the airfoil chord c. Moreover, α_{L0} is the angle of zero lift, μ_0 is a coefficient, f_1 and f_2 are auxiliary functions and $C_{M_{c/4}}$ is the pitching moment coefficient around the quarter chord.

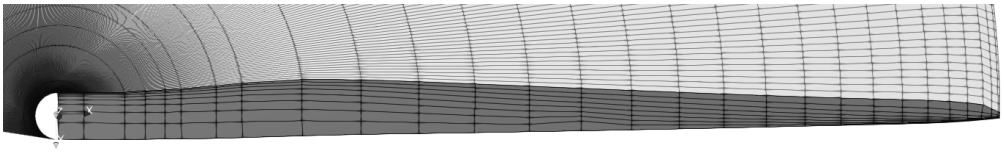


Fig. 9 Blade and wake mesh in SHARPy.

The OpenFAST discretisation includes 51 nodes. The aerodynamic module has been configured to account for tangential induction and tip and hub losses through the Prandtl model. Furthermore, BEM wake induction model has been activated (uncoupled wake-skewness option) and airfoil unsteady aerodynamics are simulated through Gonzalez's variation of Beddoes-Leishman theory [38]. Dynamic BEM and Pitt and Peters skew wake models have been tested but not reported here because they predict very large variations in loads along a revolution. This mismatch is already reported in the theory manual of AeroDyn [39].

B. Steady uniform inflow

The simplest case for wind turbine aerodynamics is the operation at constant rotation speed under steady uniform incoming wind perpendicular to the rotor plane. In this situation, incoming velocities do not vary azimuthally and,

thus, neither do blade forces. This is a steady-state situation in a frame of reference rotating with the rotor, typically the optimum for power production and loading. However, it is not the usual operating state of wind turbines because incoming flows are not uniform (shear and turbulence), steady (turbulence) or perpendicular to the rotor plane (yaw).

In the case of steady uniform flow (Fig. 10 and Table 1), both codes agree quite well in the spanwise variation of loads. The trends in SHARPy and OpenFAST are very similar agreeing on the mid-span and the tip region, showing the inherently capability of vortex method to account for tip effects. However, SHARPy predicts lower out-of-plane and higher in-plane coefficients throughout the span in comparison with OpenFAST. This is related to both the absence of viscous drag estimation in SHARPy and the geometrical changes described in section IV.A, that are very sensitive to small changes in the angle of zero lift. The rotor thrust and power estimation differ in a 6% and a 13%, respectively (Table 1).

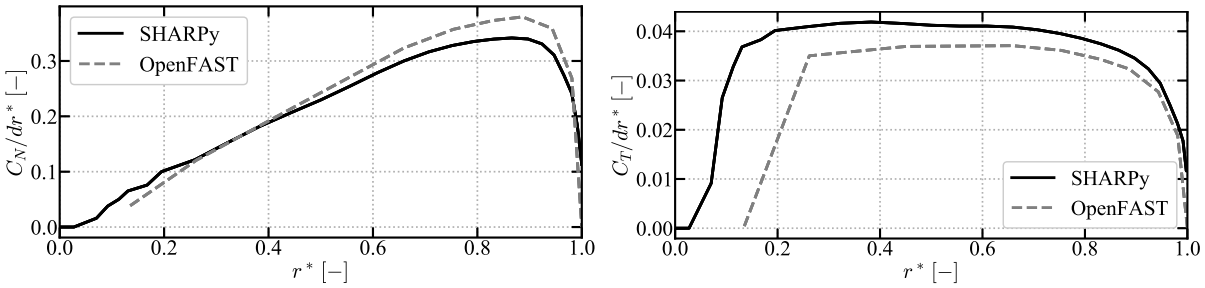


Fig. 10 Loads along the span direction in steady uniform inflow

Table 1 Loads at r^*=0.75 and rotor coefficients in steady uniform inflow

	$C_N/dr^*\|_{r^*=0.75}$ [−]	$C_T/dr^*\|_{r^*=0.75}$ [−]	C_{th} [−]	C_p [−]
SHARPy	0.33	0.040	0.62	0.51
OpenFAST	0.36	0.036	0.66	0.45

C. Shear inflow

Shear is the denomination of the variation of the wind speed with height due to the atmospheric boundary layer. It is usually approximated by a power law characterised by a certain exponent

$$U(z) = U_h\,(z/z_h)^{\gamma}\,, \tag{22}$$

where $U(z)$ is the wind speed (it takes the value of U_h at hub height), z is the height with respect to the ground and γ is the characteristic exponent of the power law. This velocity gradient will trigger the unsteady, spanwise component and spanwise variations studied in sections III.A, III.B and III.C respectively. The estimation of loads in shear wind is very important because they are always present, they are large and they appear at rotor and blade-passing frequencies which can interact with the vibrations of other parts of the system [6].

In the case of wind shear, SHARPy and OpenFAST are found to be in very good agreement (Fig. 11), considering that the differences highlighted in section IV.B are still present. Incoming wind speed is larger at the top and smaller at the bottom positions generating larger and smaller loads respectively (Fig. 11). This effect generates reduction of the average coefficients and increase of the standard deviation with varying severity along the radial position (Fig. 12) being stronger close to the tip because of the larger variations of velocity. The average normal and tangential coefficients can decrease up to a 4 %.

Fig. 13 summarises the effect of the shear exponent on the integrated rotor coefficients. The larger the shear exponent the larger the power and thrust variations along a cycle and the larger the decrease with respect to the uniform inflow.

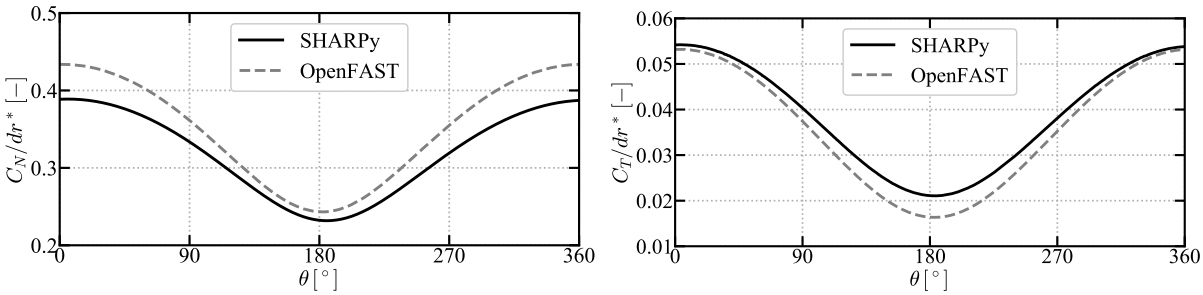


Fig. 11 Loads along a revolution for a point at r^*=0.75 for shear exponent γ=0.3

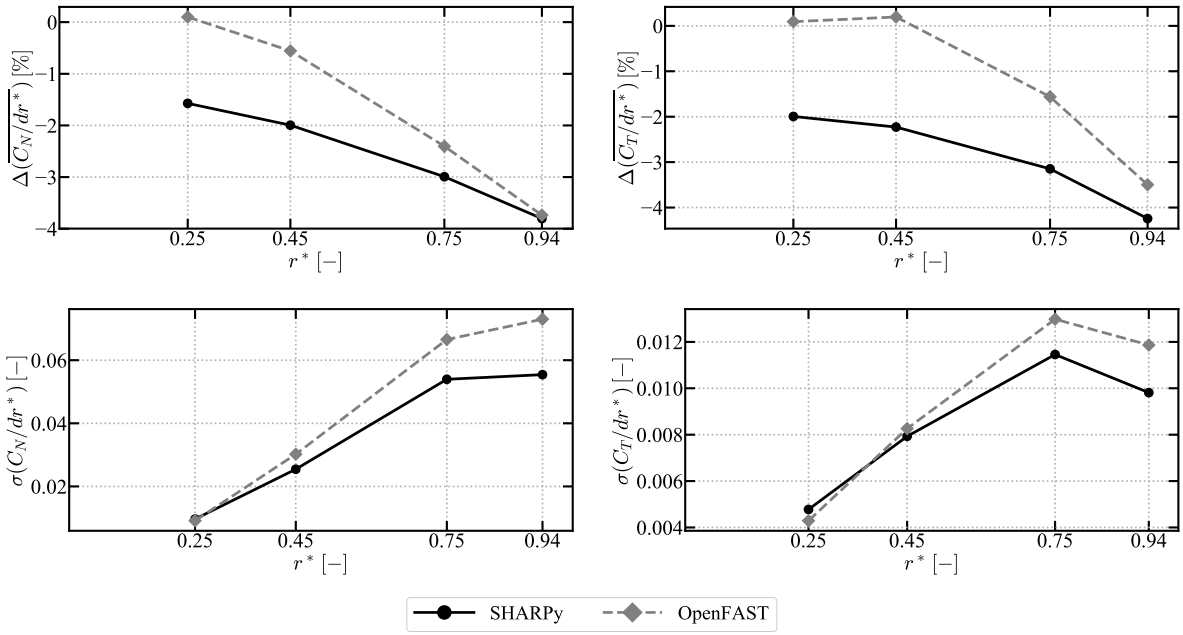


Fig. 12 Average and standard deviation of loads at different radial positions for shear exponent γ=0.3

However, due to the nonlinear wind distribution, at the highest shear exponent the decrease is slightly smaller than in the previous case.

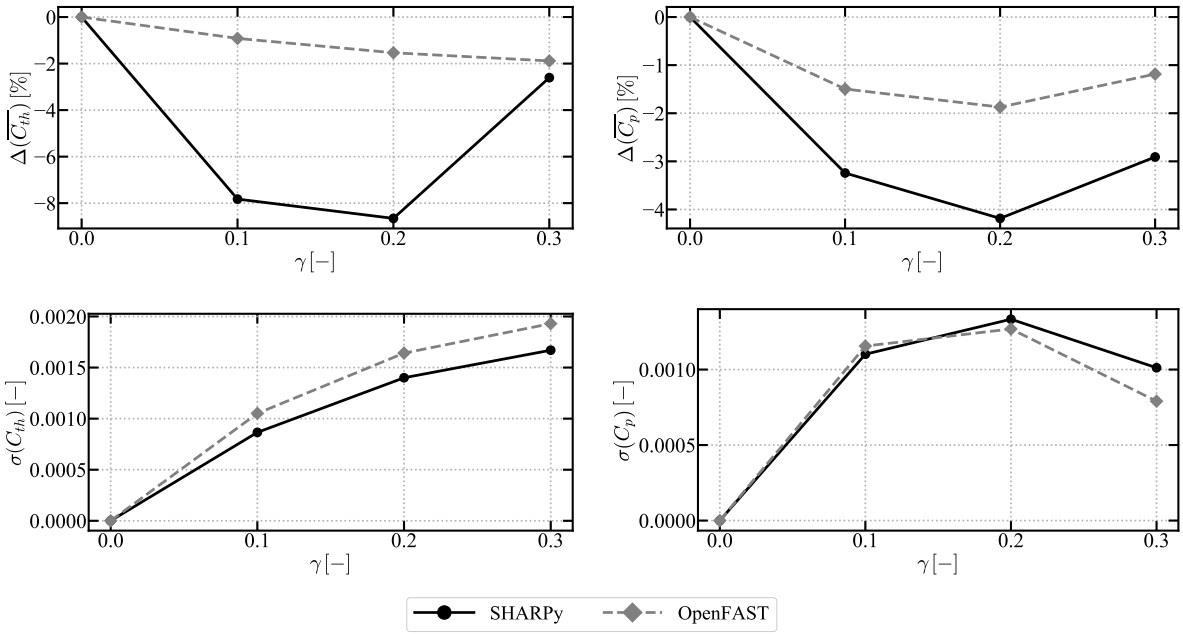


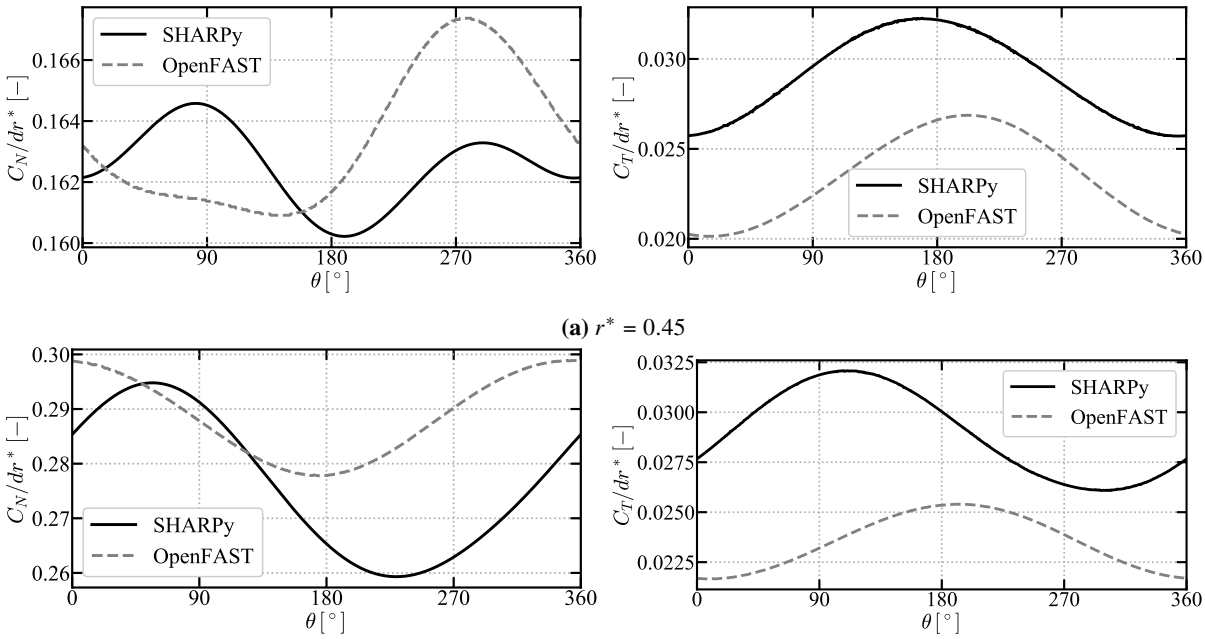
Fig. 13 Rotor coefficients for different wind shear exponents

D. Yaw inflow

Yaw cases are characterised by the existence of an incidence angle between the incoming wind speed and the rotation axis of the wind turbine in the horizontal plane. The capability of the methods to capture the effects that occur under yaw is highly related to their capability to capture the unsteady and spanwise component effects studied in sections III.A and III.B. Yaw is related with failures in the alignment mechanism and they constitute a crucial concern to estimate the load envelope of the wind turbine. To date, it has rarely been considered to be relevant to power production estimation. However, it is gaining importance due to emerging wind farm control strategies. These strategies attempt to voluntarily operate some wind turbines in yaw to reduce the influence of the wake on the downstream turbines [40].

In the presence of yaw, two effects [34] differentiate wind turbine aerodynamics from the reference case (section IV.B). The first one is the *advancing/retreating effect* and accounts for the change in angle of attack along a revolution due to the change in relative orientation between the blade and the inflow. For example, at the top position the blade rotation is in the same direction as the in-plane component of the incoming wind which increases the angle of attack with respect to the reference case. This effect generates maximum and minimum loading at $\theta = 0°$ and $\theta = 180°$ and will not create a net out-of-plane loading along one complete rotation. This effect is less noticeable near the tip because the velocity of the blade due to rotation is dominant there. The second effect is known as the *skewed wake effect* and accounts for the different distances from the blade to the shed vorticity along a revolution. The blade and the shed vorticity will be closer when the blade is in the downwind position and further away when it is in the upwind position. The closer the blade, the larger the induction and thus the lower the loads, thus, minimum and maximum occur at $\theta = 90°$ and $\theta = 270°$ and are stronger near the tips. This effect generates a net yaw moment that tends to orient the wind turbine perpendicular to the wind.

The *advancing/retreating* predicts maximum and minimum loading at $\theta = 0\,°$ and $\theta = 180\,°$ and it is dominant near the root. On the other hand, the *skewed wake* predicts maximum and minimum loading at $\theta = 90\,°$ and $\theta = 270\,°$ and it gains importance towards the tip. Fig. 14 provides an insight into these effects. In the root region (Fig. 14a), the maxima and minima are expected to occur at $\theta = 0\,°$ and $\theta = 180\,°$, which is clearly in the tangential coefficient of both solvers but not in the normal coefficient whose variations are very small. Near the tips (Fig. 14b), the *skewed wake* effect is dominant and the maxima and minima are shifted towards $\theta = 90\,°$ and $\theta = 270\,°$. This effect is well captured by SHARPy but ignored by OpenFAST.



(a) $r^* = 0.45$

(b) $r^* = 0.75$

Fig. 14 Loads for the case of yaw Ψ=30°

Azimuthal variations are further investigated in Fig. 15 which shows the positions of maxima and minima along a revolution for different spanwise locations. SHARPy coefficients near the root are close to $\theta = 0°$ or $\theta = 180°$ and evolve towards $\theta = 90°$ or $\theta = 270°$ near the tips. The largest error from this behaviour happens at the root position of the normal coefficient which is traditionally not well accounted for by vortex methods. However, OpenFAST predictions are always very close to $\theta = 0°$ or $\theta = 180°$ evidencing the absence of an adequate *skewed wake* correction.

The effect of different yaw angles in the rotor coefficients is shown in Fig. 16. There is a good agreement among the two codes which suggest that there is an important averaging effect along a revolution and that the average values are well captured by all the codes. They both predict severe thrust and power coefficient reduction with respect to the uniform inflow case that can reach 20 % and 30 %, respectively. At the same time, the two codes show an increase in the variations along a revolution as yaw increases. OpenFAST predicts smaller variations along a revolution but larger average decrease than SHARPy.

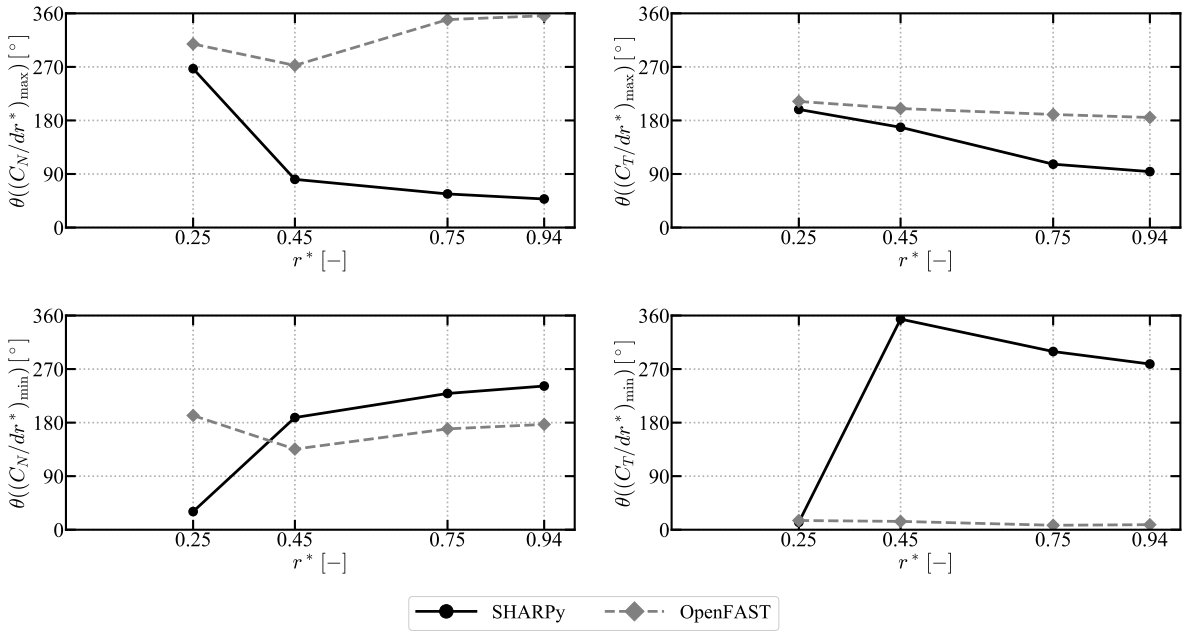


Fig. 15 Position of maxima and minima of the load coefficients along a revolution for the case of yaw Ψ=30°

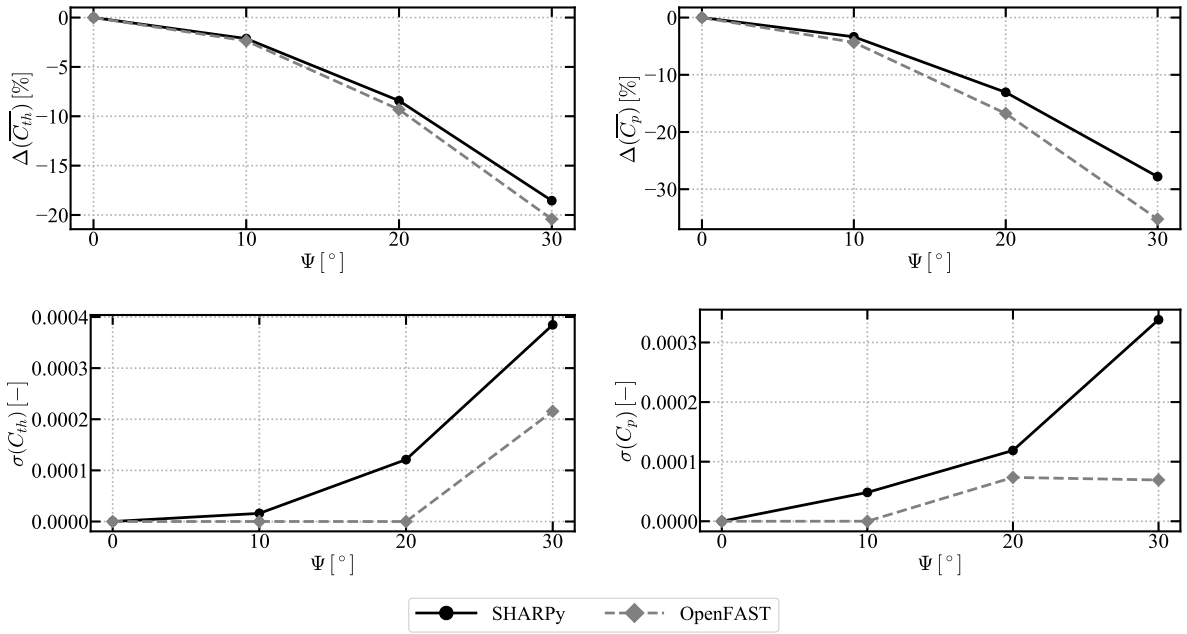


Fig. 16 Rotor coefficients for different yaw cases

E. Turbulent inflow

Finally *turbulent* wind variations in space and time are considered. They trigger the unsteady and spanwise variation effects analysed in sections III.A and III.C respectively. The loads generated under this kind of inflow are very relevant in the estimation of the fatigue life of wind turbines [6].

Here, turbulence has been generated with TurbSim [32] based on the IEC standard (Edition 3) using the IEC-KAI method with a NTM turbulence type and three levels of turbulence: A, B and C with approximately TI = 20 [%], TI = 18 [%] and TI = 16 [%], respectively. It has been generated with a time-step of 0.05 s (equivalent to 2.7 °) with no shear component.

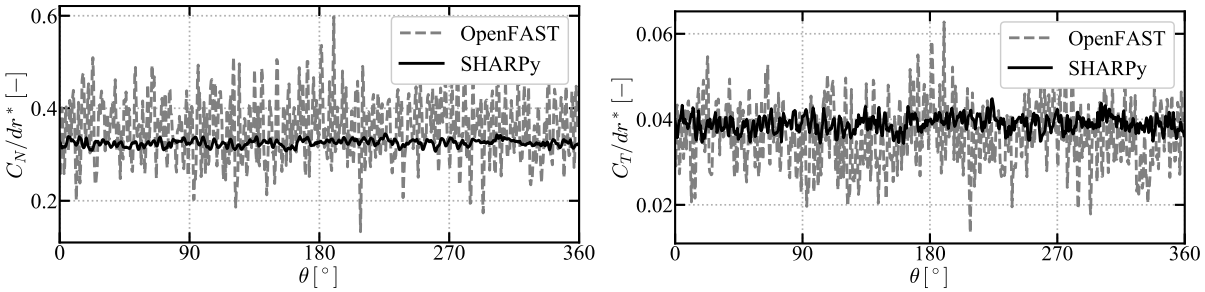


Fig. 17 Sample of load history along a revolution for a point at r^*=0.75 for turbulence level A

When average values along a revolution are considered, SHARPy and OpenFAST predict similar results (Fig. 17). In Fig. 18 the differences along the span shows that both solvers predict a decrease in average out-of-plane and in-plane coefficients smaller than one percent. However, SHARPy predicts almost no variation near the tip while OpenFAST predicts a very strong decay. Moreover, In Figure 19 both solvers predict a very low thrust and power decrease with turbulence (<0.4% and < 0.8% respectively).

However, there are very significant differences between both methods when the variations along a revolution are studied because OpenFAST is not able to account for the interaction between blade sections (section III). As it can be seen in Figure 18, the standard deviation of the loads along a revolution predicted by SHARPy is around one order of magnitude smaller that the prediction of OpenFAST. In the case of rotor coefficients, the difference is smaller due to the averaging effect, but it is still two times smaller. This highlights the importance of considering the interaction between blade sections to avoid overestimating the fluctuation of loads.

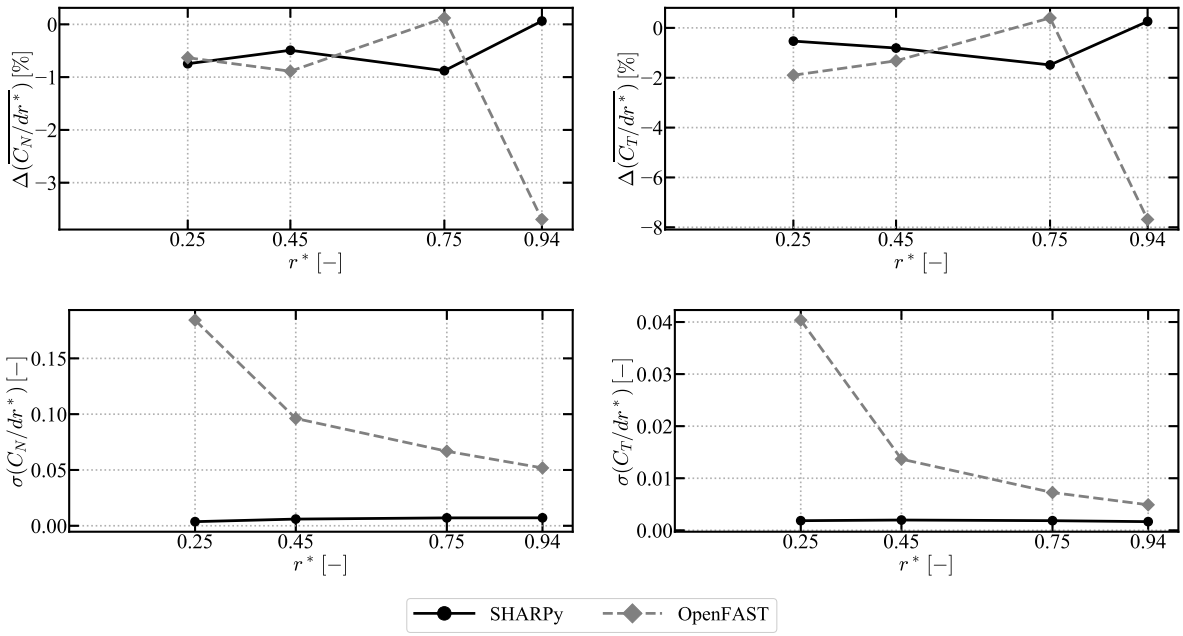


Fig. 18 Loads at different radial positions for turbulence level A

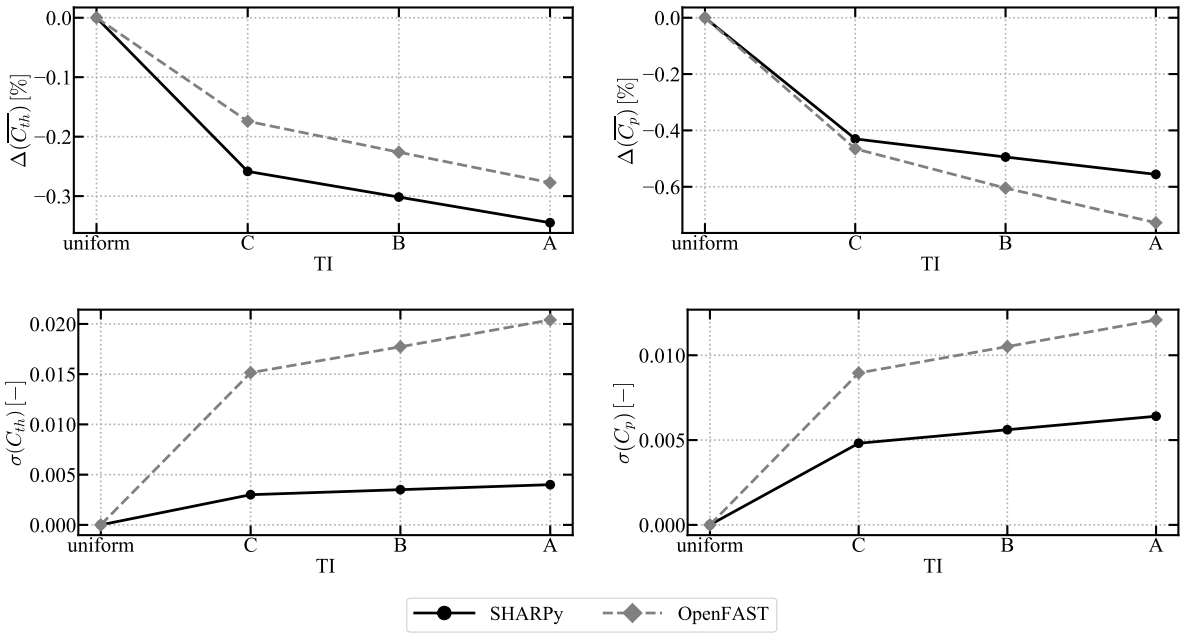


Fig. 19 Rotor coefficients for different turbulence levels

V. Concluding remarks

A new implementation of the UVLM has been verified against analytical solutions of unsteady airfoil and lifting-line theories probing its ability to capture flow unsteadiness and three-dimensional effects. Moreover, they have been used to show how unsteady aerodynamics smooth and delays the system response with respect to a steady approximation. However, only phenomena with very short characteristic time (such as flapwise bending) can trigger this unsteadiness. They have shown how the side slip of the inflow over an airfoil reduces the maximum lift coefficient and displaces it from the wing mid point. Finally, the reduction of the peak-to-peak lift and the appearance of net drag, moment and spanwise coefficient has been explained as a function of the wavelength of a sinusoidal inflow velocity varying along the span.

Both OpenFAST and SHARPy predict reasonable tendencies when accounting for azimuthal variations generated by shear. SHARPy predicts smaller variations along a cycle but larger average reduction of the mean thrust and power coefficients which can add up to 8 % and 4 % for rotor thrust and power, respectively.

In the case of yaw, only vortex methods are able to capture key flow physics for the estimation of the location of maximum and minimum loading along a cycle. However, significant averaging effect was observed which led to a good agreement in the estimation of integrated rotor coefficients among the two codes that predict a thrust and power reduction up to 20 % and 30 %, respectively, with respect to the uniform case.

In the cases of turbulence the average values along a revolution are quite coherent between both solvers: predicting coherent decay of average in-plane and out-of-plane coefficients at different blade points. Moreover, the average rotor coefficients can reach 0.4% and 0.8% for thrust and power, respectively. However, when the loads variation along a revolution are studied very important differences appear. First, in-plane and out-of-plane variations along the span are one order of magnitude smaller in the case of SHARPy estimation. When this variations are measured in rotor coefficients the difference decreases, but OpenFAST still predicts two or three times larger variations than SHARPy. This discrepancy comes from the fact that OpenFAST assumes independent blade sections while SHARPy is able to capture spanwise variations as shown for the wing case under spanwise varying inflow velocity.

In conclusion, BEM methods are accurate under simple inflow conditions, however, vortex methods have shown a good estimation of unsteady behaviour under complex inflow configurations, which are a better representation of the real operating cases of wind turbines. The present work highlights the need of higher complexity methods to study the wind turbine rotor loads in detail and the risk of using averaged load coefficients and integrated rotor coefficients that hide the discrepancies. Moreover, current AL-LES methods for the simulation of wind farms use some assumptions similar to BEM methods and constitute a field of further investigation for the authors.

Acknowledgements

This project has received funding from the European Research Council (ERC) under the European Union's Horizon 2020 research and innovation programme (grant agreement number 765579). The first author wishes to acknowledge the help of Álvaro González, Maria Aparicio and Raquel Martín from the National Renewable Energy Centre of Spain (CENER) with OpenFAST-based wind turbine computations.

References

[1] van Kuik, G. A. M., Peinke, J., Nijssen, R., Lekou, D., Mann, J., Sørensen, J. N., Ferreira, C., van Wingerden, J. W., Schlipf, D., Gebraad, P., Polinder, H., Abrahamsen, A., van Bussel, G. J. W., Sørensen, J. D., Tavner, P., Bottasso, C. L., Muskulus, M., Matha, D., Lindeboom, H. J., Degraer, S., Kramer, O., Lehnhoff, S., Sonnenschein, M., Sørensen, P. E., R. Künneke, W., Morthorst, P. E., and Skytte, K., "Long-term research challenges in wind energy – a research agenda by the European Academy of Wind Energy," *Wind Energy Science*, Vol. 1, No. 1, 2016, pp. 1–39. doi:10.5194/wes-1-1-2016.

[2] Breton, S.-P., Sumner, J., Sørensen, J. N., Hansen, K. S., Sarmast, S., and Ivanell, S., "A survey of modelling methods for high-fidelity wind farm simulations using large eddy simulation," *Philosophical Transactions of the Royal Society A: Mathematical, Physical and Engineering Sciences*, Vol. 375, No. 2091, 2017, p. 20160097. doi:10.1098/rsta.2016.0097.

[3] Hansen, M., Sørensen, J., Voutsinas, S., Sørensen, N., and Madsen, H., "State of the art in wind turbine aerodynamics and aeroelasticity," *Progress in Aerospace Sciences*, Vol. 42, No. 4, 2006, pp. 285–330. doi:10.1016/j.paerosci.2006.10.002.

[4] Schepers, J., Heijdra, J., Thomsen, K., Larsen, T., Foussekis, D., Rawlinson-Smith, R., Kraan, I., Visser, B., Øye, S., Ganander, H., Carlen, I., Voutsinas, S., Belessis, M., and Drost, L., "Verification of European wind turbine design codes, VEWTDC; Final Report," Tech. Rep. Denmark, ECN, 1 2001.

[5] Buhl, M., and Manjock, A., "A Comparison of Wind Turbine Aeroelastic Codes Used for Certification," *44th AIAA Aerospace Sciences Meeting and Exhibit*, 2006. doi:10.2514/6.2006-786.

[6] Burton, T., Sharpe, D., Jenkins, N., and Bossanyi, E., *Wind Energy Handbook*, Wiley, 2001.

[7] Beddoes, T. S., "Practical computation of unsteady lift," Tech. Rep. 2.3, Association aeronautique et astronautique de France, 1982.

[8] Pitt, D. M., and Peters, D. A., "Theoretical prediction of dynamic infow derivatives," *Vertica*, Vol. 5(1), 1983, pp. 21–34.

[9] Madsen, H. A., Sørensen, N. N., and Schreck, S., "Yaw Aerodynamics Analyzed with Three Codes in Comparison with Experiment," *41st Aerospace Sciences Meeting and Exhibit*, American Institute of Aeronautics and Astronautics, 2003. doi:10.2514/6.2003-519.

[10] Rahimi, H., Dose, B., Stoevesandt, B., and Peinke, J., "Investigation of the validity of BEM for simulation of wind turbines in complex load cases and comparison with experiment and CFD," *Journal of Physics: Conference Series*, Vol. 749, 2016, p. 012015. doi:10.1088/1742-6596/749/1/012015.

[11] Voutsinas, S. G., "Vortex methods in aeronautics: how to make things work," *International Journal of Computational Fluid Dynamics*, Vol. 20, No. 1, 2006, pp. 3–18. doi:10.1080/10618560600566059.

[12] Katz, J., and Plotkin, A., *Low-Speed Aerodynamics*, Cambridge University Press, 2001. doi:10.1017/cbo9780511810329.

[13] Simoes, F. J., and Graham, J. M. R., "Application of a free vortex wake model to a horizontal axis wind turbine," *Journal of Wind Engineering and Industrial Aerodynamics*, Vol. 39, No. 1-3, 1992, pp. 129–138. doi:10.1016/0167-6105(92)90539-m.

[14] Ramos-García, N., Sørensen, J. N., and Shen, W. Z., "Validation of a three-dimensional viscous-inviscid interactive solver for wind turbine rotors," *Renewable Energy*, Vol. 70, 2014, pp. 78–92. doi:10.1016/j.renene.2014.04.001.

[15] Sørensen, N. N., Ramos-García, N., Voutsinas, S., Jost, E., and Lutz, T., "Aerodynamics of Large Rotors: Effects of complex inflow for the AVATAR reference rotor and NM80 rotors," Tech. Rep. Stuttgart, 2017. URL `http://www.eera-avatar.eu/publications-results-and-links/index.html`.

[16] Carrión, M., Woodgate, M., Steijl, R., Barakos, G., Gómez-Iradi, S., and Munduate, X., "CFD and Aeroelastic Analysis of the MEXICO Wind Turbine," *Journal of Physics: Conference Series*, Vol. 555, 2014, p. 012006. doi:10.1088/1742-6596/555/1/012006.

[17] Drela, M., *Flight Vehicle Aerodynamics*, MIT Press Ltd, 2014.

[18] Lanzafame, R., and Messina, M., "Fluid dynamics wind turbine design: Critical analysis, optimization and application of BEM theory," *Renewable Energy*, Vol. 32, No. 14, 2007, pp. 2291–2305. doi:10.1016/j.renene.2006.12.010.

[19] "OpenFAST Documentation," , 1 2019. URL `https://openfast.readthedocs.io/en/latest/index.html`, version 1.0.

[20] Jonkman, J. M., and Buhl Jr, M. L., "FAST user's guide," Tech. Rep. NREL/EL-500-38230, NREL, 2005.

[21] Jonkman, B., and Jonkman, J., "FAST v8.16.00a-bjj," Tech. rep., NREL, 2016.

[22] Anderson, J. D., *Fundamentals of Aerodynamics*, McGraw-Hill Science/Engineering/Math, 2001.

[23] Ng, B. F., Palacios, R., Kerrigan, E. C., Graham, J. M. R., and Hesse, H., "Aerodynamic load control in horizontal axis wind turbines with combined aeroelastic tailoring and trailing-edge flaps," *Wind Energy*, Vol. 19, No. 2, 2016, pp. 243–263. doi:10.1002/we.1830.

[24] Murua, J., Palacios, R., and Graham, J. M. R., "Applications of the unsteady vortex-lattice method in aircraft aeroelasticity and flight dynamics," *Progress in Aerospace Sciences*, Vol. 55, 2012, pp. 46–72. doi:10.1016/j.paerosci.2012.06.001.

[25] Del Carre, A., Goizueta, N., Muñoz Simón, A., Maraniello, S., Palacios, R., and Otsuka, K., "ImperialCollegeLondon/sharpy: v1.0.1," , 2019. doi:10.5281/ZENODO.3544841.

[26] Del Carre, A., and Palacios, R., "Efficient Time-Domain Simulations in Nonlinear Aeroelasticity," *AIAA Scitech 2019 Forum*, 2019. doi:10.2514/6.2019-2038.

[27] Ng, B. F., Hesse, H., Palacios, R., Graham, J. M. R., and Kerrigan, E. C., "Aeroservoelastic state-space vortex lattice modeling and load alleviation of wind turbine blades," *Wind Energy*, Vol. 18, No. 7, 2014, pp. 1317–1331. doi:10.1002/we.1752.

[28] Hesse, H., and Palacios, R., "Consistent structural linearisation in flexible-body dynamics with large rigid-body motion," *Computers & Structures*, Vol. 110-111, 2012, pp. 1–14. doi:10.1016/j.compstruc.2012.05.011.

[29] Géradin, M., and Cardona, A., *Flexible Multibody Dynamics: A Finite Element Approach*, Wiley, 2001.

[30] Simpson, R. J., and Palacios, R., "Numerical aspects of nonlinear flexible aircraft flight dynamics modeling," *54th AIAA/ASME/ASCE/AHS/ASC Structures, Structural Dynamics, and Materials Conference*, 2013. doi:10.2514/6.2013-1634.

[31] Roesler, B. T., and Epps, B. P., "Discretization Requirements for Vortex Lattice Methods to Match Unsteady Aerodynamics Theory," *AIAA Journal*, Vol. 56, No. 6, 2018, pp. 2478–2483. doi:10.2514/1.j056400.

[32] Jonkman, B. J., and Kilcher, L., "TurbSim User's Guide: Version 1.06.00," Tech. Rep. Report, 2012.

[33] Sieros, G., "Redesign of the AVATAR RWT rotor," Tech. rep., NTUA, 2017. URL `http://www.eera-avatar.eu/publications-results-and-links/index.html`.

[34] Snel, H., and Schepers, J. G., "Joint investigation of dynamic inflow effects and implementation of an engineering method," Tech. Rep. ECN-C–94-107, ECN, 1995.

[35] Cheng, H. K., "Lifting-Line Theory of Oblique Wings," *AIAA Journal*, Vol. 16, No. 11, 1978, pp. 1211–1213. doi:10.2514/3.61033.

[36] Schepers, J., Boorsma, K., Sørensen, N., Voutsinas, S., Sieros, G., Rahimi, H., Heisselmann, H., Jost, E., Lutz, T., Maeder, T., González, A., Ferreira, C., Stoevesandt, B., Barakos, G., Lampropoulos, N., Croce, A., and Madsen, J., "Final results from the EU project AVATAR: Aerodynamic modelling of 10 MW wind turbines," *Journal of Physics: Conference Series*, Vol. 1037, 2018, p. 022013. doi:10.1088/1742-6596/1037/2/022013.

[37] Abbott, I. H., *Theory of wing sections : including a summary of airfoil data*, Dover, New York, 1959.

[38] González, A., and Munduate, X., "Unsteady modelling of the oscillating S809 aerofoil and NREL phase VI parked blade using the Beddoes-Leishman dynamic stall model," *Journal of Physics: Conference Series*, Vol. 75, 2007, p. 012020. doi:10.1088/1742-6596/75/1/012020.

[39] Moriarty, P., and Hansen, A., "AeroDyn Theory Manual," Tech. Rep. TP-500-36881, NREL, 2005.

[40] Gebraad, P. M. O., Teeuwisse, F. W., van Wingerden, J. W., Fleming, P. A., Ruben, S. D., Marden, J. R., and Pao, L. Y., "Wind plant power optimization through yaw control using a parametric model for wake effects-a CFD simulation study," *Wind Energy*, Vol. 19, No. 1, 2014, pp. 95–114. doi:10.1002/we.1822.